

# Higher-order Dirac sonic crystals

Chunyin Qiu (✉ [cyqiu@whu.edu.cn](mailto:cyqiu@whu.edu.cn))

Wuhan University <https://orcid.org/0000-0002-4318-3420>

Huahui Qiu

Wuhan University

Meng Xiao

Wuhan University <https://orcid.org/0000-0002-2087-3007>

Fan Zhang

University of Texas at Dallas <https://orcid.org/0000-0003-4623-4200>

---

## Research Article

**Keywords:** topological phases, sonic crystals, classical waves

**Posted Date:** December 29th, 2020

**DOI:** <https://doi.org/10.21203/rs.3.rs-126317/v1>

**License:**  This work is licensed under a Creative Commons Attribution 4.0 International License.

[Read Full License](#)

---

# Higher-order Dirac sonic crystals

Huahui Qiu,<sup>1</sup> Meng Xiao,<sup>1</sup> Fan Zhang,<sup>2</sup> and Chunyin Qiu<sup>1\*</sup>

<sup>1</sup>Key Laboratory of Artificial Micro- and Nano-Structures of Ministry of Education and School of Physics and Technology, Wuhan University, Wuhan 430072, China

<sup>2</sup>Department of Physics, University of Texas at Dallas, Richardson, Texas 75080, USA

**Abstract:** Discovering new topological phases of matter is a major theme in fundamental physics and materials science<sup>1,2</sup>. Dirac semimetal features isolated fourfold linear band crossings, i.e., Dirac points, and provides an exceptional platform for exploring topological phase transitions under symmetry breaking<sup>3</sup>. Recent theoretical studies<sup>4,5</sup> have revealed that a three-dimensional Dirac semimetal can harbor fascinating hinge states, a high-order (HO) topological manifestation not known before. However, realization of such a HO Dirac phase in experiment is yet to be achieved, not to mention the fascinating hinge states, although candidate solid-state materials have been suggested<sup>5</sup>. Here we propose a minimum model to construct a *spinless* HO Dirac semimetal protected by  $C_{6v}$  symmetry. By breaking different symmetries, this parent phase transitions into a variety of novel topological phases including HO topological insulator, HO Weyl semimetal, and HO nodal-ring semimetal. Furthermore, for the first time, we experimentally realize this unprecedented HO topological phase in a sonic crystal and unambiguously present the smoking-gun observation of the desired hinge states via momentum-space spectroscopy and real-space visualization. Our findings may offer new opportunities to manipulate classical waves such as sound and light.

Topological phases of matter have been one of the most active research fields since the discovery of topological insulators (TI)<sup>1-3</sup>. One fundamental feature of such fascinating phases is the bulk implication of protected boundary modes, dubbed bulk-boundary correspondence. Recently, tremendous efforts have been devoted to predicting higher-order (HO) topological phases that admit unconventional bulk-boundary correspondence<sup>4-11</sup>. Unlike the conventional (first-order) topological phases that feature gapless modes at boundaries of one dimension lower, i.e., co-dimension  $d_c = 1$ , the hallmark of HO topological phases is the existence of gapless modes at boundaries of co-dimension  $d_c > 1$ , e.g., corner modes of a two-dimensional (2D) system and hinge modes of a three-dimensional (3D) system. In understanding such HO topological phases and their topological responses, spatial symmetries often play a critical role, in addition to time-reversal and/or particle-hole symmetries.

Nontrivial HO topology has been predicted not only in gapped insulators<sup>6-11</sup> but also in gapless semimetals<sup>4,5,12-15</sup>. These new HO members greatly enrich the already diverse spectrum of topological phases of matter. Interestingly for a HO Dirac semimetal, its gapped 2D slices may be classified into two HO topologically distinct insulators, for which the transition occurs exactly at the Dirac points<sup>4,5</sup>. Similar topological transitions also emerge in HO Weyl semimetals<sup>12-15</sup>. Such features lead to the presence of fascinating one-dimensional (1D) hinge modes connecting the projected Dirac or Weyl nodes, a robust manifestation of the HO bulk-hinge correspondence. This hallmark is markedly different from the surface Fermi arcs previously observed in conventional topological semimetals<sup>3,16-19</sup>.

To date there have been extensive studies of various HO topological phases in condensed matter and materials physics<sup>4-15,20-26</sup>, ranging from solid-state materials to ultra-cold atoms, from photonics to acoustics, etc. In particular, the artificial crystals for classical waves have been demonstrated to be exceptional platforms for exploring those otherwise elusive topological phases, benefiting from their macroscopically more controllable structures and less demanding measurements<sup>27,28</sup>. A variety of HO TIs have been ingeniously realized in such classical systems

soon after their theoretical predictions<sup>20,21,23-26</sup>. However, little experimental progress has been made toward the HO topological nodal phases, despite that a family of solid-state materials has been suggested to realize a spin-orbit-coupled Dirac semimetal phase<sup>5</sup>. In this work, we theoretically propose a simple scheme to construct a *spinless* HO Dirac semimetal, as a parent phase for a novel family of HO topological phases including TI, Weyl semimetal, and nodal-ring semimetal, experimentally realize it in a 3D Dirac sonic crystal, and unambiguously present the first smoking-gun observation of its fascinating hinge modes.

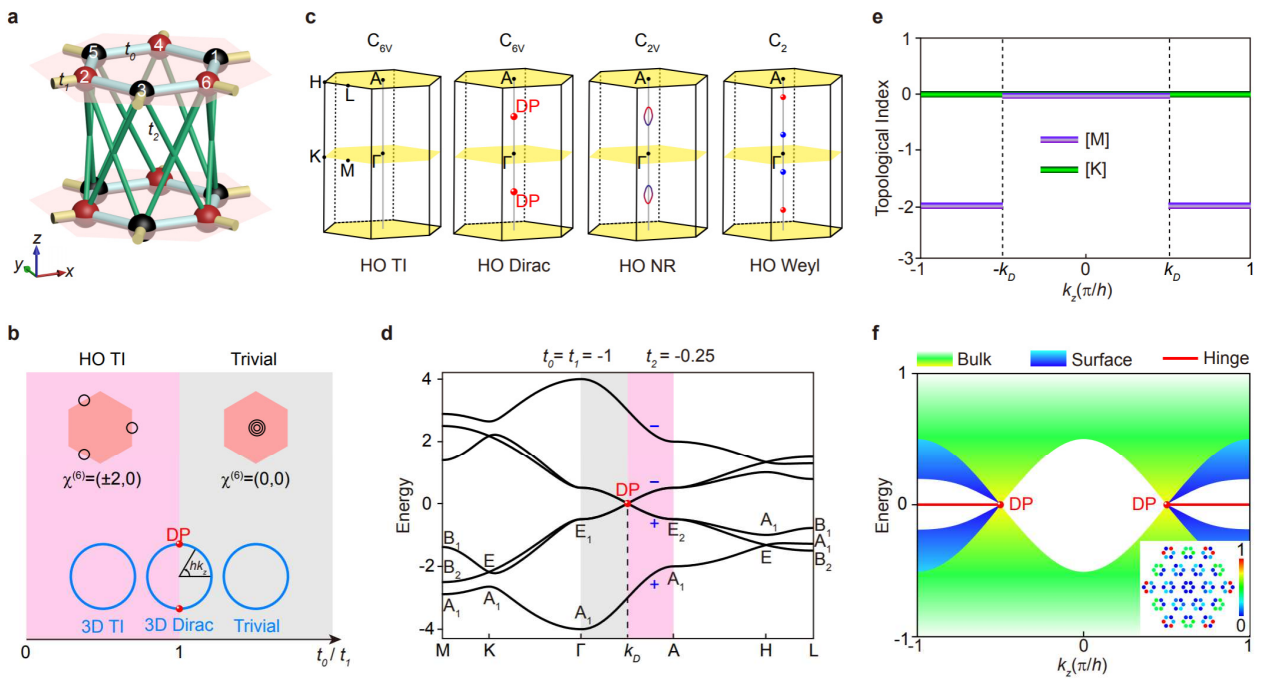


**Fig. 1 | Tight-binding model for constructing 3D HO topological phases.** **a**, 3D tight-binding model. The six orbitals in each unit cell form two different sublattices (colored spheres).  $t_0$  is the intra-cell coupling, and  $t_1$  and  $t_2$  are the in-plane and out-of-plane inter-cell couplings. **b**, Reduced topological phase diagram for the 2D monolayer system. The trivial and HO TI phases have different topological indices  $\chi^{(6)} = ([M], [K])$  and Wannier centers (black circles) for the lower three bands. The blue circles sketch three possible evolution scenarios of the  $k_z$  slices when  $hk_z$  varies from  $-\pi$  to  $\pi$ . **c**, Multiple 3D HO topological phases realized by our model, including TI and Dirac, Weyl, and nodal-ring (NR) semimetals. The colored points (rings) label the HO Dirac or Weyl points (NRs) that come in pairs. **d**, Bulk band structure for a set of couplings that features HO Dirac points. The bands are labeled by the  $C_{6v}$  irreducible

representations at high-symmetry momenta and the  $C_2$  parities along the  $\Gamma A$  line. **e**, Topological indices  $\chi^{(6)} = ([M], [K])$  plotted as a function of  $k_z$ . **f**, Hinge-projected spectrum calculated for an infinitely long hexagonal prism. It features zero-energy hinge modes (red lines) connecting the projected Dirac points. Inset: Typical in-plane eigenfields of the hinge modes.

We first present in Fig. 1a a minimal tight-binding model for our designed 3D system that can exhibit multiple HO topological phases. Each unit cell includes six spinless orbitals with intra-cell couplings  $t_0$ , inter-cell couplings  $t_{1,2}$ , and vanishing onsite energies. The in-plane and out-of-plane lattice constants are  $a$  and  $h$ , respectively. Each monolayer forms a triangular lattice, i.e., a  $\sqrt{3} \times \sqrt{3}$  superstructure of an original hexagonal lattice, and can be modeled by a Hamiltonian  $H_{2D} = t_0 H_0 + t_1 H_1$ .  $H_0$  is a constant matrix with its nontrivial entries representing the nearest-neighbour couplings within the same unit cell.  $H_1(\mathbf{k}_{\parallel}) = \bigoplus_{i=1}^3 [\cos(\mathbf{k}_{\parallel} \cdot \mathbf{a}_i) \sigma_x - \sin(\mathbf{k}_{\parallel} \cdot \mathbf{a}_i) \sigma_y]$  corresponds to couplings between the neighbouring unit cells, where  $\mathbf{k}_{\parallel}$  is the in-plane Bloch wavevector,  $\sigma_{x,y}$  are the Pauli matrices coupling the two sublattices, and  $\mathbf{a}_i$  are the 2D primitive lattice vectors  $\mathbf{a}_1 = (a, 0)$  and  $\mathbf{a}_{2,3} = (-\frac{a}{2}, \mp \frac{\sqrt{3}a}{2})$ . In addition to the  $C_{6v}$  and time-reversal symmetries,  $H_{2D}$  enjoys a chiral symmetry since the six orbitals lie in two decoupled sublattices. Recently, it has been demonstrated<sup>23,29</sup> that the nontrivial HO topology of such a 2D insulator with  $C_6$  symmetry can be characterized by two topological invariants  $\chi^{(6)} = ([M], [K])$ . Specifically, the index  $[M]$  (or  $[K]$ ) is a measure of the difference in  $C_2$  (or  $C_3$ ) representation for the valence-band states at the high-symmetry momenta  $\Gamma$  and  $M$  (or  $K$ ). Figure 1b shows a reduced phase diagram for our monolayer model<sup>29</sup>. Whereas the  $C_3$  symmetry operator commutes with the chiral symmetry operator yielding a trivial  $C_3$ -invariant  $[K] = 0$ <sup>23</sup>, the  $C_2$  symmetry relates the two different sublattices and can give rise to nontrivial HO band topology. For  $0 < t_0/t_1 < 1$ , the  $C_2$ -invariant  $[M] = \pm 2$ , where  $\pm$  denote the signs of  $t_1$ . In sharp contrast to the trivial phase (i.e.,  $[M] = 0$  for  $t_0/t_1 > 1$ ) with Wannier centers at the unit cell center, the nontrivial phase with Wannier centers at the sides of the unit cell exhibits zero-energy corner modes in a finite-sized sample (*see Supplementary Information*). In

particular, at the phase boundary  $t_0/t_1 = 1$ , the bulk gap closes and the 2D system features a fourfold degenerate Dirac point at the  $\Gamma$  point, as an accidental degeneracy between two inequivalent 2D irreducible  $C_{6v}$  representations; the two double degeneracies at the K and K' points of the original hexagonal lattice are folded into the  $\Gamma$  point of its  $\sqrt{3} \times \sqrt{3}$  triangular superlattice.

Our 3D system can also be modeled by the Hamiltonian  $H_{2D}$  if  $t_0$  is replaced by  $t_{eff} = t_0 + 2t_2 \cos(hk_z)$ . As  $hk_z$  varies from  $-\pi$  to  $\pi$ , the relative intra-cell to inter-cell coupling  $t_{eff}/t_1$  experiences a circle of radius  $|2t_2/t_1|$  around the origin  $(t_0/t_1, 0)$ , as illustrated in Fig. 1b. When the origin is in the nontrivial phase side and the radius is sufficiently small, e.g., the HO TI monolayers are barely coupled, any  $k_z$  slice realizes the 2D HO TI phase, and the stacked system is a 3D HO TI (with perfectly flat zero-energy hinge states due to the chiral symmetry). On the contrary, the stacked system is topologically trivial when the origin is in the trivial phase side and the radius is sufficiently small. Intriguingly, when the circle traverses the phase boundary, one time-reversal pair of Dirac points emerge in the rotational axis. To exemplify this Dirac semimetal phase, we consider the case with  $t_0 = t_1 = -1$  and  $t_2 = -0.25$ . Figure 1d plots the bulk band structure that features one Dirac point at  $k_D = \frac{\pi}{2h}$  in the high-symmetry line  $\Gamma A$ . (The other Dirac point is at  $k_z = -k_D$ .) As shown in Fig. 1e, the  $C_2$ -invariant is nontrivial ( $[M] = -2$ ) for the momentum range  $|k_z| > |k_D|$ , while the  $C_3$ -invariant  $[K]$  vanishes everywhere. The nontrivial topological invariants  $\chi^{(6)} = (-2, 0)$  for  $|k_z| > |k_D|$  implies the existence of hinge states connecting the hinge projections of the two Dirac points, since all the  $k_z$  slices within  $|k_z| > |k_D|$  host corner modes. This is further confirmed by the hinge spectrum of an infinitely long hexagonal prism in Fig. 1f, where there exist six symmetric 1D hinge states at exactly zero energy (because of the chiral symmetry). Clearly, the derived Dirac semimetal, sharply different from the conventional Dirac semimetals, has a HO nature.

Remarkably, the HO Dirac points are protected by the  $C_{6v}$  symmetry. In Fig. 1d, the Dirac point is an accidental crossing point in the  $\Gamma A$  line between two pairs of bands that have opposite  $C_2$

parities, and each pair itself forms a 2D irreducible representation of the  $C_{3v}$  point group. When the  $C_3$  symmetry is broken, the Dirac point evolves into a zero-energy nodal ring (NR) in the intact mirror plane. When both the  $C_3$  and mirror symmetries are broken, the Dirac point splits into two Weyl points in the  $\Gamma A$  line. We stress that all these 3D HO topological phases summarized in Fig. 1c are unprecedented. Evidently, the symmetry protections of the HO bulk nodes are sharply different from their conventional (first-order) counterparts. At boundary, while gapless surface states only exist for the HO Weyl and NR semimetals, characteristic hinge states do exist for all the four HO topological phases due to the presence of the nontrivial  $C_2$ -invariant. Hereafter, we will focus on the HO Dirac semimetal, since it is a parent phase for all the other HO topological phases listed in Fig. 1c (*see Supplementary Information*).

We further emulate our 3D tight-binding model in an acoustic system, in which cavity resonators and narrow tubes are used respectively to mimic orbitals and couplings<sup>24,25</sup>. In addition to identifying the bulk Dirac points, we confirm the HO nature by obtaining the  $k_z$ -resolved [M] index and the flat hinge states at the resonant frequency (*see Supplementary Information*). Importantly, the HO Dirac points can be realized in any (more general) acoustic structure that features the same space group and topological invariants, as shown numerically and experimentally in a sonic crystal below. Comparing with the cavity-tube system, this design relaxes the chiral symmetry, which is inessential for protecting the hinge states, and possesses unique merits, such as broad bulk bands and dispersive hinge states (due to the absence of resonance) and convenient experimental detections (due to the improved structural porosity and connectivity).

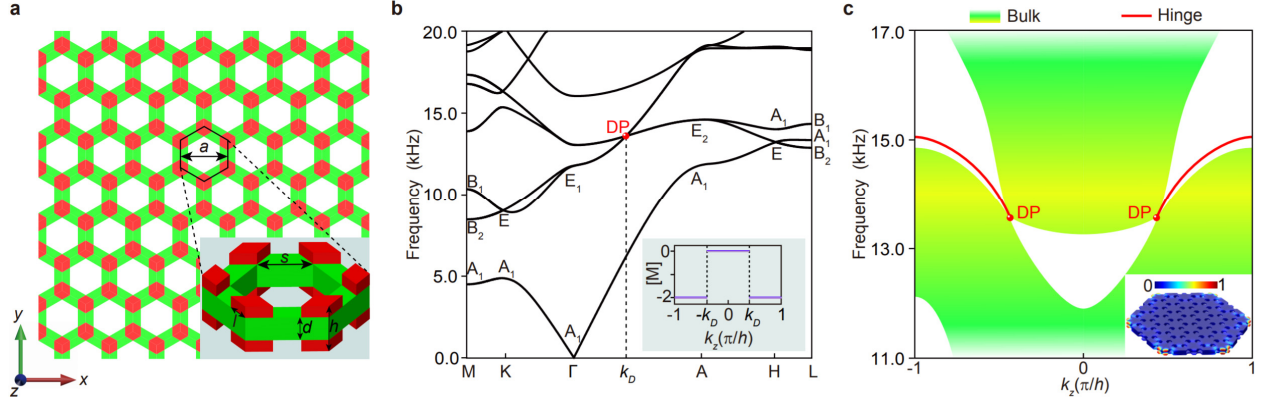


**Fig. 2 | Acoustic realization of the HO (type-II) Dirac points.** **a**, In-plane geometry and structure of our 3D Dirac sonic crystal. **b**, Bulk band structure along high-symmetry directions. At the high-symmetry points, the lowest three bands are characterized by the same irreducible representations to the lowest three bands in Fig. 1d, with a nontrivial  $[M]$  index for  $|k_z| > k_D$  (inset). **c**, Hinge-projected spectrum. Inset: Pressure amplitude distribution of the hinge states of 14.86 kHz simulated in a small-size system.

Figure 2a displays the structure of our layered Dirac sonic crystal. The in-plane and out-of-plane lattice constants are  $a = 27.7$  mm and  $h = 9.6$  mm, respectively. Each layer is formed by a hard plate (of thickness  $d = 4.8$  mm) perforated with a triangle lattice of hexagonal holes (of sidelength  $s = 10.7$  mm). The layers are connected by hexagonal pillars of sidelength  $l = 5.3$  mm. The whole plate-pillar structure (colored in Fig. 2a) is assumed to be acoustically rigid, and we consider the airborne sound in the remaining space. Our full-wave simulations are performed by using COMSOL Multiphysics (*see Methods*). Figure 2b plots the bulk band structure along high-symmetry lines. Clearly, there exists a fourfold degenerate Dirac point at frequency  $\sim 13.7$  kHz and  $k_D \sim 0.4\pi/h$  along the  $\Gamma A$  line. Note that the Dirac cone, dubbed type-II<sup>3,30,31</sup>, is strongly tilted since the chiral symmetry is not present. After inspecting the eigenfields of the lowest three bands at the high-symmetry points, we find that the acoustic system features the same irreducible representations to those of the tight-binding model in Fig. 1d. As such, the  $C_2$ -invariant  $[M]$  is nontrivial for the momentum range  $|k_z| > k_D$  (see the inset of Fig. 2b), which is suggestive of a hinge state connecting the time-reversal pair of projected Dirac

points through  $|k_z| > k_D$ . This is indeed confirmed by the hinge spectrum simulated for a finite-sized sample, as shown in Fig. 2c. Moreover, the inset of Fig. 2c shows the strong hinge localization of the hinge states. Note that the absence of chiral symmetry enables broadband hinge states that can be easily frequency-resolved in our airborne sound experiments below.

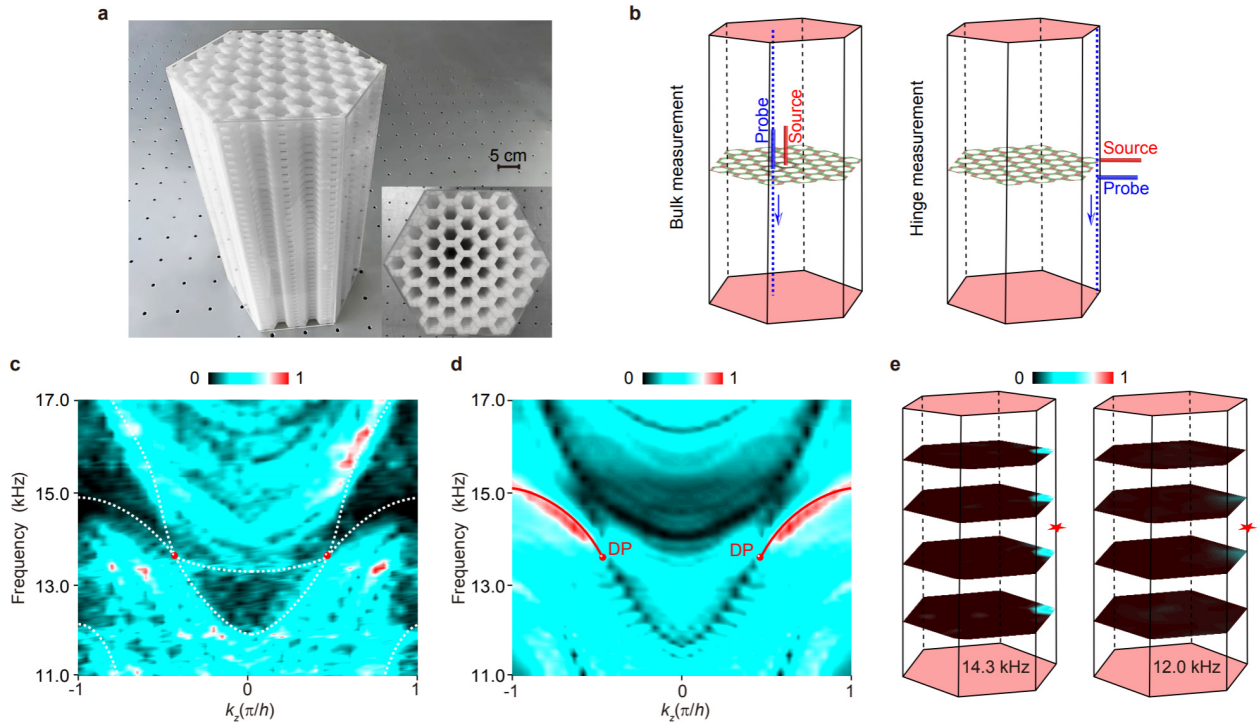


**Fig. 3 | Experimental observation of the HO Dirac points and 1D hinge states.** **a**, Side and top views of our experimental sample. **b**, Schematics of our bulk and hinge measurements. The blue dotted line indicates the scanning path in each case. **c**, Bulk spectrum (color scale) excited by a sound source inserted into the middle of the sample interior. The white dashed lines sketch the boundaries of the projected bulk bands extracted from Fig. 2c. **d**, Hinge spectrum (color scale) excited by a sound source placed in the middle of the sample hinge, which reproduces well the simulated hinge states (red line) in Fig. 2c. **e**, Pressure amplitude distributions scanned in four equidistant planes of the sample, exemplified at 14.3 kHz and 12.0 kHz. The red star labels the position of the sound source.

Finally, we perform airborne sound experiments to conclusively identify the Dirac points and hinge states, the two defining signatures of the HO Dirac sonic crystal. Figure 3a shows our

experimental sample, fabricated precisely via 3D printing with photosensitive resin. It consists of 49 unit cells in the  $x$ - $y$  plane and 40 layers along the  $z$  direction. Acrylic plates are closely pasted on the six side surfaces to mimic the hard boundary condition implemented in the simulation. We first measure the bulk bands of our Dirac sonic crystal. As illustrated in the left panel of Fig. 3b, we insert a point-like sound source into the middle of the sample from its top facet and scan the pressure distribution along a vertical hole adjacent to the sound source. Figure 3c presents the 1D Fourier transform of the measured data, with red and black indicating strong and weak amplitudes, respectively. The observed bulk spectrum captures the full-wave simulated boundaries of the projected bulk bands in Fig. 2c and exhibits the expected band touching around each predicted Dirac point.

Next, we measure the 1D hinge spectrum. We position the sound source in the middle of one hinge and scan the pressure distribution along the hinge (*see Method*), as illustrated in the right panel of Fig. 3b. Exhibiting as the brightest signals in Fig. 3d, the dispersive hinge states emanate from the two projected Dirac points and match well with the full-wave simulation in Fig. 2c. Essentially, the presence of protected 1D hinge states instead of 2D surface states is the HO manifestation of our Dirac sonic crystal, which is markedly different from the conventional (first-order) Dirac semimetals with surface arc states<sup>3,16,17</sup>. In addition to the spectroscopy measurement, we also scan the pressure field pattern over the entire sample with the same hinge excitation. Figure 3e shows the pressure amplitude profiles in four equidistant planes of the sample at two typical frequencies. As expected, at 14.3 kHz a strong localization of the pressure field is observed around the sample hinge where the sound source is positioned. This forms a sharp contrast to the weak field distribution displayed at 12.0 kHz, a frequency away from the hinge states. Such extremely localized HO hinge modes are anticipated to have potential applications, such as acoustic sensing and energy trapping.

In conclusion, we have proposed a series of unprecedented 3D HO topological phases with a simple scheme, in which the parent phase possesses  $C_{6v}$  symmetry-protected Dirac points and

hinge states. In particular, we have successfully fabricated a HO Dirac sonic crystal and unambiguously identified the smoking-gun signatures, i.e., the Dirac points and hinge states, by performing full-wave simulations and airborne sound experiments. The design of our sonic crystal enables us to observe not only the hinge states in frequency-resolved spectroscopy but also their spatial localization in pressure-field distributions. Not only is this HO Dirac sonic crystal sharply different from the conventional solid-state Dirac semimetals that are characterized by surface Fermi arcs<sup>3,16,17</sup>, but it is also markedly different from the recently achieved non-symmorphic Dirac sonic crystals that feature symmetry-enforced Dirac points and quad-helicoid surface arcs<sup>32,33</sup>. Last but not at least, our scheme for achieving spinless 3D HO topological phases can be readily generalized to other classical wave systems such as photonic crystals with similar space groups.

## Methods

**Numerical simulations.** All full-wave simulations were performed by using a commercial solver package (COMSOL Multiphysics). The photosensitive resin material used for fabricating samples was modeled as acoustically rigid in the airborne sound environment, given the extremely mismatched acoustic impedance between resin and air. The air density  $1.29 \text{ kg/m}^3$  and the sound speed  $343 \text{ m/s}$  were used to solve the eigen-problems in Figs. 2b and 2c. Specifically, the bulk band structure in Fig. 2b was obtained by imposing Bloch boundary condition along all directions. The hinge spectrum in Fig. 2c was simulated for an infinitely long hexagonal prism, i.e., with rigid boundary condition for its side surfaces and Bloch boundary condition along the  $z$  direction.

**Experimental measurements.** Our experimental sample (Fig. 3a), which has the geometry of a regular hexagonal prism, was fabricated via the 3D printing technique with a nominal fabrication error  $\sim 0.2 \text{ mm}$ . To detect the bulk information, a broadband point-like sound source, launched from a subwavelength-sized tube, was directly inserted into the middle of the sample from its top facet, and a  $1/4$  inch microphone (B&K Type 4187) was used to scan the pressure information through a vertical hole adjacent to the middle one (see the left panel in Fig. 3b), with a spatial step

of  $h = 9.6$  mm. Both the amplitude and phase information of the input and output signals was recorded and frequency-resolved with a multi-analyzer system (B&K Type 3560B). The bulk spectrum in Fig. 3c was obtained by performing 1D Fourier transform of the measured data. Special treatment was implemented to detect the hinge modes that are strongly localized at the hinges (see the inset of Fig. 2c). Specifically, the cover plate was perforated with 40 equidistant side holes (of radius 0.4 mm) in the vicinity of a sample hinge. The point source was fixed in the middle side hole, and the microphone was inserted into the side holes and moved to scan the pressure information along the hinge (see the right panel in Fig. 3b). The side holes not in use were sealed during measurements. The hinge spectrum in Fig. 3d was obtained by performing 1D Fourier transform of the measured data. To demonstrate the field distributions in Fig. 3e, additional data measured from other vertical holes were supplemented.

### **Acknowledgements**

C.Q. is supported by the National Natural Science Foundation of China (Grant No. 11890701), the Young Top-Notch Talent for Ten Thousand Talent Program (2019-2022), and the Fundamental Research Funds for the Central Universities (Grant No. 2042020kf0209). M.X. is supported by the National Natural Science Foundation of China (Grant No. 11904264). F.Z. is supported by the UT Dallas Research Enhancement Fund.

### **Author contributions**

C.Q. conceived the idea and supervised the project. H.Q. did the simulations and experiments. C.Q., H.Q., M.X., and F.Z. analyzed the data and wrote the manuscript. All authors contributed to scientific discussions of the manuscript.

### **Author information**

Correspondence and requests for materials should be addressed to C.Q. (cyqiu@whu.edu.cn).

## References

1. Hasan, M. Z. & Kane, C. L. Colloquium: topological insulators. *Rev. Mod. Phys.* **82**, 3045-3067 (2010).
2. Qi, X. L. & Zhang, S. C. Topological insulators and superconductors. *Rev. Mod. Phys.* **83**, 1057-1110 (2011).
3. Armitage, N. P., Mele, E. J. & Vishwanath, A. Weyl and Dirac semimetals in three-dimensional solids. *Rev. Mod. Phys.* **90**, 015001 (2018).
4. Lin, M. & Hughes, T. L. Topological quadrupolar semimetals. *Phys. Rev. B* **98**, 241103 (2018).
5. Wieder, B. J. et al. Strong and fragile topological Dirac semimetals with higher-order Fermi arcs, *Nat. Commun.* **11**, 627 (2020).
6. Zhang, F., Kane, C. L. & Mele, E. J. Surface state magnetization and chiral edge states on topological insulators. *Phys. Rev. Lett.* **110**, 046404 (2013).
7. Benalcazar, W. A., Bernevig, B. A. & Hughes, T. L. Quantized electric multipole insulators. *Science* **357**, 61-66 (2017).
8. Benalcazar, W. A., Bernevig, B. A. & Hughes, T. L. Electric multipole moments, topological multipole moment pumping, and chiral hinge states in crystalline insulators. *Phys. Rev. B* **96**, 245115 (2017).
9. Langbehn, J., Peng, Y., Trifunovic, L., Oppen, F. & Brouwer, P. W. Reflection-symmetric second-order topological insulators and superconductors. *Phys. Rev. Lett.* **119**, 246401 (2017).
10. Song, Z., Fang, Z. & Fang, C. (d-2)-dimensional edge states of rotation symmetry protected topological states. *Phys. Rev. Lett.* **119**, 246402 (2017).
11. Schindler, F. et al. Higher-order topological insulators. *Sci. Adv.* **4**, eaat0346 (2018).
12. Ezawa, M. Higher-order topological insulators and semimetals on the breathing kagome and pyrochlore lattices. *Phys. Rev. Lett.* **120**, 026801 (2018).
13. Ghorashi, S., Li, T. & Hughes, T. L. Higher-order Weyl Semimetals. arXiv:2007.02956v1.
14. Wang, H., Lin, Z., Jiang, B., Guo, G. & Jiang, J. Higher-order Weyl Semimetals. *Phys. Rev. Lett.* **125**, 146401 (2020).

15. Wei, Q. et al. Higher-order topological semimetal in phononic crystals, arXiv:2007.03935.
16. Wang, Z. et al. Dirac semimetal and topological phase transitions in  $A_3\text{Bi}$  ( $A = \text{Na}, \text{K}, \text{Rb}$ ). *Phys. Rev. B* **85**, 195320 (2012).
17. Xu, S.-Y. et al. Observation of Fermi arc surface states in a topological metal. *Science* **347**, 294-298 (2015).
18. Xu, S.-Y. et al. Discovery of a Weyl fermion semimetal and topological Fermi arcs. *Science* **349**, 613-617 (2015).
19. Lv, B. Q. et al. Experimental discovery of Weyl semimetal TaAs. *Phys. Rev. X* **5**, 031013 (2015).
20. Serra-Garcia, M. et al. Observation of a phononic quadrupole topological insulator. *Nature* **555**, 342-345 (2018).
21. Peterson, C. W., Benalcazar, W. A., Hughes, T. L. & Bahl, G. A quantized microwave quadrupole insulator with topological protected corner states. *Nature* **555**, 346-350 (2018).
22. Imhof, S. et al. Topoelectrical circuit realization of topological corner states. *Nat. Phys.* **14**, 925-929 (2018).
23. Noh, J. et al. Topological protection of photonic mid-gap defect modes. *Nat. Photon.* **12**, 408-415 (2018).
24. Xue, H., Yang, Y., Gao, F., Chong, Y. & Zhang, B. Acoustic higher-order topological insulator on a kagome lattice. *Nat. Mater.* **18**, 108-112 (2019).
25. Ni, X., Weiner, M., Alù, A. & Khanikaev, A. B. Observation of higher-order topological acoustic states protected by generalized chiral symmetry. *Nat. Mater.* **18**, 113-120 (2019).
26. Zhang, X. et al. Second-order topology and multidimensional topological transitions in sonic crystals. *Nat. Phys.* **15**, 582-588 (2019).
27. Ozawa, T. et al. Carusotto, Topological photonics. *Rev. Mod. Phys.* **91**, 015006 (2019).
28. Ma, G., Xiao, M. & Chan, C. T. Topological phases in acoustic and mechanical systems. *Nat. Rev. Phys.* **1**, 281-294 (2019).
29. Benalcazar, W. A., Li, T. & Hughes, T. L. Quantization of fractional corner charge in symmetric higher-order topological crystalline insulators, *Phys. Rev. B* **99**, 245151 (2019).

30. Xu, Y., Zhang, F. & Zhang, C. Structured Weyl Points in Spin-Orbit Coupled Fermionic Superfluids, *Phys. Rev. Lett.* **115**, 265304 (2015).
31. Soluyanov, A. A. et. al, Type-II weyl semimetals, *Nature* **527**, 495-498 (2015).
32. Cheng, H., Sha, Y., Liu, R., Fang, C., & Lu, L. Discovering topological surface states of Dirac points. *Phys. Rev. Lett.* **124**, 104301 (2020).
33. Cai, X. et al. Symmetry-enforced three-dimensional Dirac phononic crystals. *Light Sci. Appl.* **9**, 38 (2020).

# Figures

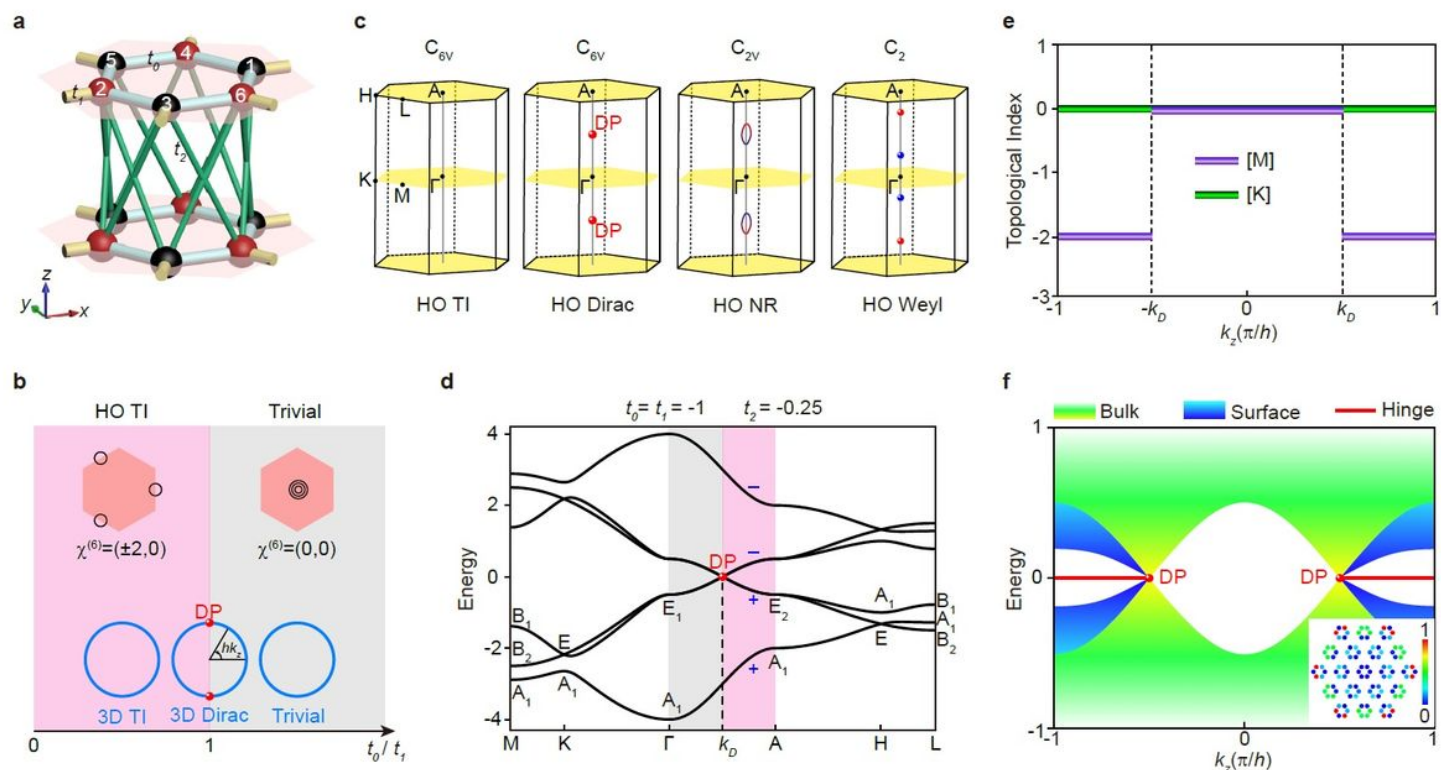


**Figure 1**

Tight-binding model for constructing 3D HO topological phases. (see manuscript file for full caption)

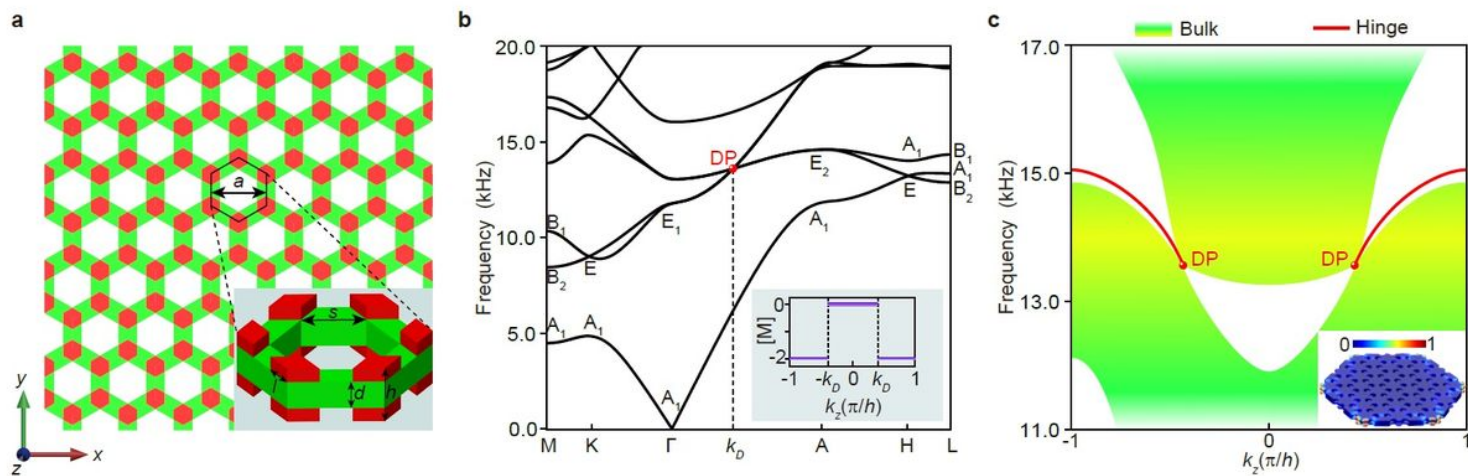


**Figure 2**

Acoustic realization of the HO (type-II) Dirac points. (see manuscript file for full caption)

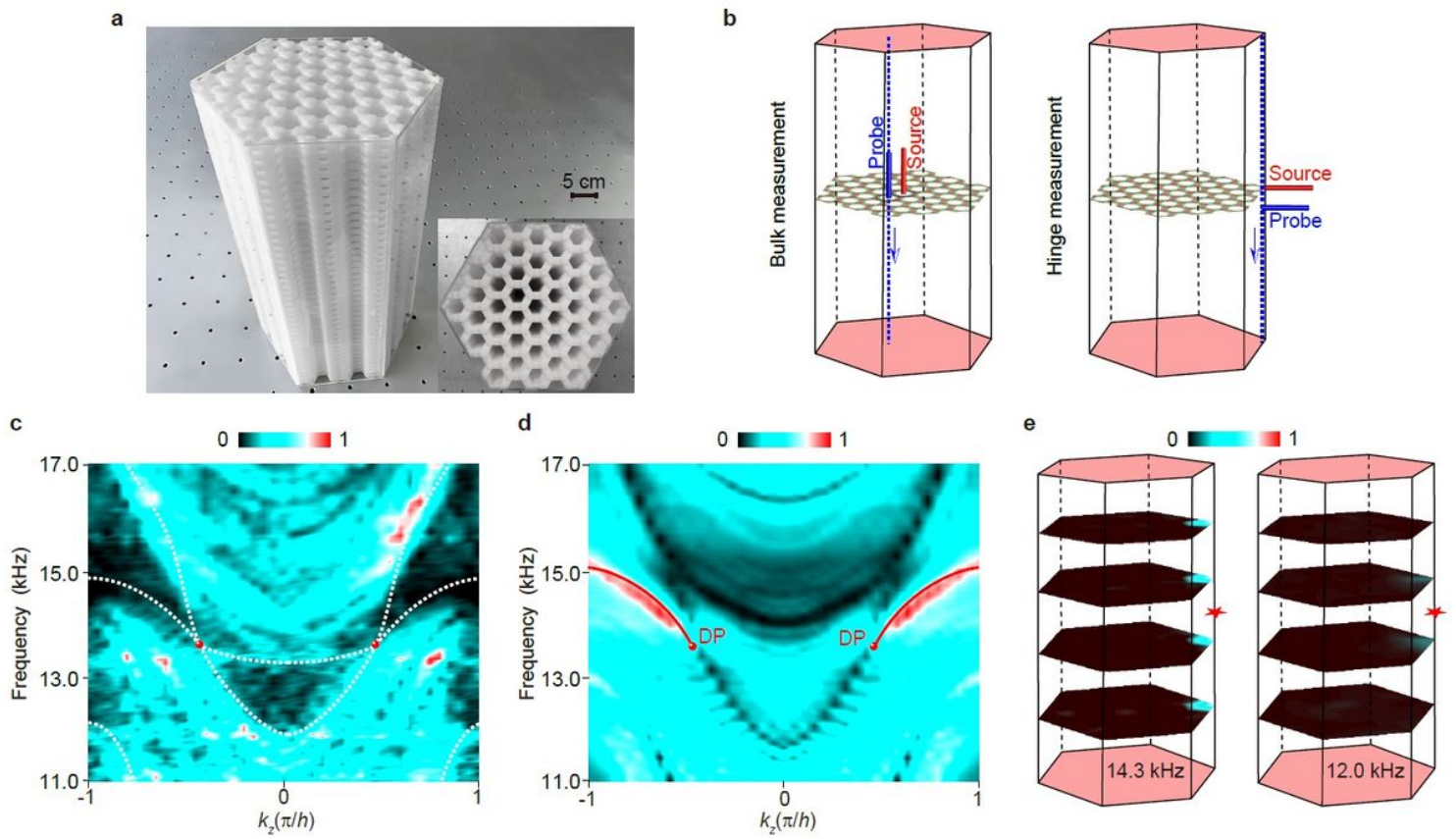


**Figure 3**

Experimental observation of the HO Dirac points and 1D hinge states.(see manuscript file for full caption)

## Supplementary Files

This is a list of supplementary files associated with this preprint. Click to download.

- [SupplementaryInformation.pdf](#)